Vortex Formation Near an Iris in a Rectangular Waveguide

RICHARD W. ZIOLKOWSKI AND J. BRIAN GRANT

Abstract —The generalized dual-series approach to the capacitive and inductive iris waveguide problems is presented. Currents on the iris and plots of the fields and power flow in the vicinity of the iris are given for the capacitive iris case. It is found that vortices form in the iris region when higher order scattered modes are present. The formation of these vortices and their properties will be described in this paper.

I. INTRODUCTION

THE ANALYSIS of the electromagnetic fields in the vicinity of a waveguide discontinuity is a classic microwave-engineering problem, for which many different methods of solution have been suggested during the past 40 years. These include integral and singular integral equation approaches [1]–[7], modal analyses [8], [9], modified residue-calculus techniques [10], variational calculations [11]–[14], method-of-moment treatments [15]–[17], and equivalent circuit formulations [18]–[20].

In a few exceptional cases, exact solutions have been found. In general, however, this is not possible and some degree of approximation must be introduced. These approximate methods are applicable to a wide range of problems and can produce sufficiently accurate results for most purposes. On the other hand, solutions to canonical problems are valuable because they provide a means to study, in detail, basic scattering phenomena. Moreover, accurate solutions of this type provide standards to which general numerical code results can be compared. In addition, they lead to general engineering analysis and design "rules of thumb" for more general geometries and to the development of improved numerical techniques, especially near the discontinuities where those methods may encounter difficulties.

In this paper, we will introduce the generalized dual-series (GDS) approach to rectangular waveguide iris problems. This method was introduced in [21]–[23] as it applies to the mixed boundary value problems that characterize the coupling of electromagnetic energy through apertures. It is based upon the solution to the Riemann–Hilbert problem of complex variable theory and allows one to obtain essentially analytical solutions to a large family of canonical problems.

In contrast to most standard techniques, the GDS approach does not require an expansion of the field in the aperture. Only the expansions of the fields on both sides of the iris are considered. It thus avoids all relative convergence problems [24], [25]. Moreover, it naturally incorporates the (singular) behavior of the fields and currents near the edge of the iris. The GDS approach also allows one to treat *directly* the dual-series systems, which are obtained from the enforcement of the electromagnetic boundary conditions in the iris plane, rather than by transforming to a spectral domain, as is necessary for the modified residue-calculus technique. Similarly, it is related to the singular integral equation method, although it provides an analytical and numerical capability not available with the latter. As a consequence, it represents an attractive alternative to the solution of many of the problems proposed by Lewin for the singular integral equation methods. Analogous to the philosophy raised in [26] and [27], a technique that accelerates the convergence of the current and field series is utilized in the GDS approach. The asymptotic behavior of the solution coefficients is identified and used to produce analytically summed series that recover the singular behavior of those physical quantities near the edge of the iris.

This effort represents a generalization of earlier work by K. F. Casey [28], [29], which solved the dual-series systems with a Jacobi polynomial inversion scheme introduced by Sneddon [30] for potential theory problems and only dealt with the susceptance calculation. The Riemann–Hilbert approach has proven to be much more straightforward and robust. Furthermore, the results presented below go well beyond the usual calculation of the susceptance. We provide the currents on the iris and the fields throughout the waveguide, especially near the iris, for a variety of incident wavelengths and iris configurations. We have found that electromagnetic vortices are formed near the iris. In analogy with fluid flow near an obstacle, increasing the frequency (corresponding to an increase in the Reynolds number) leads to an increase in the number of vortices. The formation of the vortices and their effects on power flow past the iris will be described below.

II. PROBLEM FORMULATION

The problem configuration is shown in Fig. 1. The dimensions of the waveguide are a across and b high. A vertical iris of height c is located at $z = 0$. The z direction
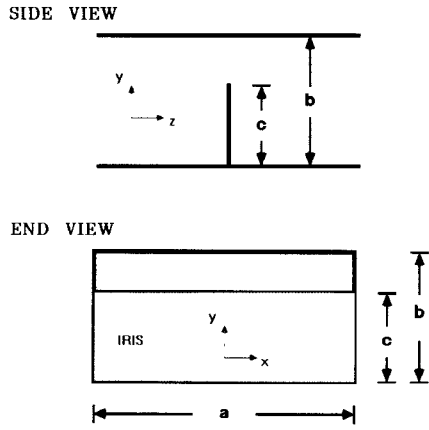
SIDE VIEW

END VIEW

Fig. 1. Capacitive iris problem geometry.

is taken along the length of the guide, x along its width, and y along its height. The incident wave arrives at the iris from the negative z direction. Because the iris is assumed to be uniform across the guide, the problem is actually two-dimensional; there is no scattering in the transverse direction.

A. Dual-Series Derivation

The incident and scattered fields are first expressed in terms of eigenmodes or, simply, the modes of the waveguide. It will then be shown that enforcing the electromagnetic boundary conditions leads to a dual-series system that can be reduced to an equivalent Riemann–Hilbert problem which can be solved as outlined by Ziolkowski in [22]. Although the formulation of the solution is carried through for both the capacitive and the inductive iris problems, only the capacitive iris case is solved explicitly and the corresponding results presented and discussed. The solution of the inductive iris case follows in a straightforward manner from the one presented below and is outlined briefly in Appendix I.

Without any loss of generality, we deal only with single-moded excitations and choose to express the fields in terms of modes that are either TE with respect to x: TE$_x$ ($E_x = 0$) or TM with respect to x: TM$_x$ ($H_x = 0$) to facilitate treating either the capacitive or the inductive iris case, respectively. In particular, we assume that a mode (l, p) which has the tangential field components

TE_x Case:

$$H_x^{\text{inc}} = S_{lp}^{\text{inc}} \sin(l\pi x/a) \cos(p\pi y/b) e^{-i\gamma_{lp}z}$$

$$E_y^{\text{inc}} = -\frac{\omega\mu}{k^2 - \left(\dfrac{l\pi}{a}\right)^2} \gamma_{lp} S_{lp}^{\text{inc}} \sin(l\pi x/a)$$

$$\cdot \cos(p\pi y/b) e^{-i\gamma_{lp}z}$$

TM_x Case:

$$E_x^{\text{inc}} = T_{lp}^{\text{inc}} \cos(l\pi x/a) \sin(p\pi y/b) e^{-i\gamma_{lp}z}$$

$$H_y^{\text{inc}} = \frac{\omega\epsilon}{k^2 - \left(\dfrac{l\pi}{a}\right)^2} \gamma_{lp} T_{lp}^{\text{inc}} \cos(l\pi x/a) \sin(p\pi y/b) e^{-i\gamma_{lp}z}$$

is incident upon the iris. In contrast to standard treatments, we will assume that these fields exist throughout the waveguide. This avoids several coefficient redefinitions and, hence, greatly simplifies the presentation. The time factor $e^{i\omega t}$ is understood and suppressed throughout this paper. Correspondingly, the scattered fields are written as

TE_x Case:

$$H_x^s = \sum_{m=0}^{\infty} \text{sgn}(z) S_{lm} \sin(l\pi x/a) \cos(m\pi y/b) e^{-i\gamma_{lm}|z|}$$

$$E_y^s = -\sum_{m=0}^{\infty} \frac{\omega\mu}{k^2 - \left(\dfrac{l\pi}{a}\right)^2} \gamma_{lm} S_{lm} \sin(l\pi x/a)$$

$$\cdot \cos(m\pi y/b) e^{-i\gamma_{lm}|z|}$$

TM_x Case:

$$E_x^s = \sum_{m=0}^{\infty} T_{lm} \cos(l\pi x/a) \sin(m\pi y/b) e^{-i\gamma_{lm}|z|}$$

$$H_y^s = \sum_{m=0}^{\infty} \frac{\omega\epsilon}{k^2 - \left(\dfrac{l\pi}{a}\right)^2} \text{sgn}(z) \gamma_{lm} T_{lm} \cos(l\pi x/a)$$

$$\cdot \sin(m\pi y/b) e^{-i\gamma_{lm}|z|}.$$

The definition of the propagation factor

$$\gamma_{lm} = \begin{cases} \left[k^2 - \left(\dfrac{l\pi}{a}\right)^2 - \left(\dfrac{m\pi}{b}\right)^2 \right]^{1/2} \\ \qquad\qquad\qquad \text{for propagating modes} \\ -i\left[\left(\dfrac{l\pi}{a}\right)^2 + \left(\dfrac{m\pi}{b}\right)^2 - k^2 \right]^{1/2} \\ \qquad\qquad\qquad \text{for evanescent modes} \end{cases}$$

guarantees the proper decay away from the iris.

Enforcing the electromagnetic boundary conditions $E_{\text{tan}} = 0$ *on the iris* and H_{tan} *continuous across the aperture of the iris*, the following sets of equations are respectively obtained:

$$\sum_{m=0}^{\infty} \gamma_{lm} S_{lm} \sin(l\pi x/a) \cos(m\pi y/b)$$

$$= -S_{lp}^{\text{inc}} \sin(l\pi x/a) \cos(p\pi y/b) \qquad (0 \leqslant y < c)$$

$$\sum_{m=0}^{\infty} T_{lm} \cos(l\pi x/a) \sin(m\pi y/b)$$

$$= -T_{lp}^{\text{inc}} \cos(l\pi x/a) \sin(p\pi y/b) \qquad (0 \leqslant y < c)$$

$$\sum_{m=0}^{\infty} S_{lm} \sin(l\pi x/a) \cos(m\pi y/b) = 0 \qquad (c < y \leqslant b)$$

$$\sum_{m=0}^{\infty} \gamma_{lm} T_{lm} \cos(l\pi x/a) \sin(m\pi y/b) = 0 \qquad (c < y \leqslant b).$$

Projecting out the x variation in all the boundary condition equations gives rise to two uncoupled sets of equa-

tions.

$$\sum_{m=0}^{\infty} S_{lm}\cos(m\pi y/b) = 0 \qquad (c < y \leqslant b) \qquad (1a)$$

$$\sum_{m=0}^{\infty} \gamma_{lm}S_{lm}\cos(m\pi y/b) = -S_{lp}^{\mathrm{inc}}\cos(p\pi y/b)$$
$$(0 \leqslant y < c) \qquad (1b)$$

$$\sum_{m=0}^{\infty} \gamma_{lm}T_{lm}\sin(m\pi y/b) = 0 \qquad (c < y \leqslant b) \qquad (2a)$$

$$\sum_{m=0}^{\infty} T_{lm}\sin(m\pi y/b) = -T_{lp}^{\mathrm{inc}}\sin(p\pi y/b)$$
$$(0 \leqslant y < c). \qquad (2b)$$

Each set comprises a dual-series problem. The first, eqs. (1), corresponds to the capacitive iris case; the second, eqs. (2), corresponds to the inductive iris case.

B. Dual-Series Solution

Consider the capacitive iris case. To make the correspondence to the results in [21]–[23], the angles $\phi = \pi y/b$, and $\Theta = \pi c/b$ and the terms

$$A_m = \begin{cases} \dfrac{1}{2}S_{l|m|} & \text{for } m \neq 0 \\ S_{l0} & \text{for } m = 0 \end{cases} \qquad (3)$$

$$\tau_m = \frac{ib}{\pi}\gamma_{l|m|} \qquad (4)$$

$$f_m = -\frac{ib}{2\pi}S_{l|m|}^{\mathrm{inc}}\delta_{mp} \qquad (5)$$

$$f(\phi) = \sum_{m=-\infty}^{\infty} f_m e^{im\phi} \qquad (6)$$

where Kronecker's $\delta_{mp} = 1$ if $m = p$ and 0 otherwise, are introduced to reduce the dual series (1) to the form

$$\sum_{m=-\infty}^{\infty} A_m e^{im\phi} = 0 \qquad (|\phi| > \Theta) \qquad (7a)$$

$$\sum_{m=-\infty}^{\infty} A_m\tau_m e^{im\phi} = f(\phi) \qquad (|\phi| < \Theta). \qquad (7b)$$

The *static* components of these terms (their small kb behavior) can be extracted by introducing the functions χ_m so that

$$\tau_m = \begin{cases} -\xi & \text{for } m = 0 \\ |m|(1+\chi_m) & \text{for } m \neq 0. \end{cases} \qquad (8)$$

This means for $m \neq 0$ that

$$\chi_m = \sqrt{1 - \left[1 - \left(\frac{l\pi}{ka}\right)^2\right]\left(\frac{kb}{m\pi}\right)^2} - 1.$$

Clearly, χ_m goes to zero as $(kb)^2$ in the static limit. Moreover, χ_m behaves like $(kb/m)^2$ for large m, i.e., for finite kb: $\lim_{|m|\to\infty}\chi_m \sim O(|m|^{-2})$. Thus, $\tau \sim |m|$ for $kb \ll$

1 or for $|m| \to \infty$. The resultant dual-series equations

$$\sum_{m=-\infty}^{\infty} A_m e^{im\phi} = 0 \qquad (|\phi| > \Theta) \qquad (9a)$$

$$\sum_{m=-\infty}^{\infty} A_m|m|(1+\chi_m)e^{im\phi} = f(\phi) \qquad (|\phi| < \Theta) \qquad (9b)$$

then conform to the ones treated in [22]. As described there and briefly in Appendix I, it yields the infinite linear system for the solution coefficients

$$x_m = \xi A_0 V_m^0 + \sum_{n=-\infty}^{\infty} V_m^n\left(f_n - \frac{|n|}{n}\chi_n x_n\right)$$
$$+ x_{-1}P_m(\cos\Theta) \qquad (10a)$$

$$-A_0 = \xi A_0 W^0 + \sum_{n=-\infty}^{\infty} W^n\left(f_n - \frac{|n|}{n}\chi_n x_n\right) - 2Sx_{-1}$$
$$(10b)$$

where

$$x_m = mA_m. \qquad (10c)$$

This system uniquely defines the desired modal coefficients. The coefficients V_m^n, W^0, W^n, and S are all simply combinations of Legendre's polynomials $P_m(\cos\Theta)$ and are given in Appendix II. Note that in the static limit where $\chi_m \to 0$, the solution coefficients (10) are the *exact* solutions of the associated "static" dual-series problem (9). This is in distinct contrast with Marcuvitz's "equivalent quasi-static method" [12, p. 153] where "· · · no attempt is made in practice to obtain the formally possible exact solution; · · ·" In the nonstatic case, the component proportional to χ_m is treated like a forcing term which is of order m^{-2} smaller than the static piece. Since the static pieces or, equivalently, the large m terms are responsible for the edge singularity, the solution of the "static" dual-series problem contains all of the information about the edge behavior of the "nonstatic" problem.

III. NUMERICAL IMPLEMENTATION

The solution system (10) is an infinite set of equations representing a Fredholm equation of the second kind which has the form

$$x_m + \sum_{n=-\infty}^{\infty} \Lambda_{mn}x_n = \sum_{n=-\infty}^{\infty} \Gamma_{mn}f_n$$

$$A_0 = \sum_{n=-\infty}^{\infty}\sum_{m\neq 0} \frac{(-)^m}{m}\Lambda_{mn}x_n - \sum_{n=-\infty}^{\infty}\sum_{m\neq 0} \frac{(-)^m}{m}\Gamma_{mn}f_n.$$

This infinite linear system can be treated in several ways. The approach developed by Johnson and Ziolkowski [21] is systematic and has proved to be very efficient. Because Λ_{mn} rapidly approaches zero for large values of n and only f_p and f_{-p} are nonzero for single-moded excitation, truncation of Λ_{mn} for $|n|$ greater than some value N can be justified rigorously. Typically, reasonable convergence

is achieved with

$$N \sim \frac{10}{\pi} \sqrt{(kb)^2 - \left(\frac{lb}{a}\right)^2}.$$

This truncation eliminates x_n in the sums for $|n| > N$. Solving by Gauss elimination (or some similar technique), the remaining $2N + 1$ by $2N + 1$ square system of linear equations

$$x_m + \sum_{n=-N}^{N} \Lambda_{mn} x_n = G_{mp} \qquad (11a)$$

$$A_0 = \sum_{n=-N}^{N} \sum_{m \neq 0} \frac{(-)^m}{m} \Lambda_{mn} x_n - \sum_{m \neq 0} \frac{(-)^m}{m} G_{mp} \qquad (11b)$$

where

$$G_{mp} = \sum_{n=-\infty}^{\infty} \Gamma_{mn} f_n \equiv \Gamma_{mp} f_p + \Gamma_{m(-p)} f_{-p} \qquad (11c)$$

and where $m = -N, -N+1, \cdots, +N$ yields good numerical approximations for the coefficients $A_0, x_{\pm 1}, \cdots, x_{\pm N}$. Additional coefficients x_m for $M \geq |m| > N$ are easily and accurately generated with (11a). As N approaches infinity, this approximate scheme becomes exact.

The electric and magnetic fields and the current induced on the iris may be readily computed from their modal expansions once the solution coefficients A_0 and $A_m = x_m/m$ ($m \neq 0$) are known. However, alternate expressions are particularly useful in increasing the rate of convergence of these sums and in studying their behavior near the edge of the iris. They are described below. They are constructed by introducing an *asymptotic* (large m) form of the solution coefficients x_m

$$\tilde{x}_m = \kappa_1 P_m + \kappa_2 P_{m+1} \qquad (12)$$

and a slight variation of it

$$\bar{x}_m = \kappa_1 P_m + \kappa_2 \frac{m}{m+1} P_{m+1}. \qquad (12')$$

With

$$F_n = f_n - \frac{|n|}{n} \chi_n x_n$$

the terms

$$\kappa_1 = \frac{1}{2}\left[\xi A_0 \cos\Theta + \sum_{n=-N}^{N} F_n P_{n+1} + 2x_{-1}\right] \qquad (12a)$$

$$\kappa_2 = -\frac{1}{2}\left[\xi A_0 + \sum_{n=-N}^{N} F_n P_n\right]. \qquad (12b)$$

Note that the argument of the Legendre polynomials, which is always $\cos\Theta$, is suppressed for notational convenience. To obtain (12), for instance, we have taken in (10a) an asymptotic form of the coefficients V_m^n

$$\tilde{V}_m^n = \frac{1}{2}[P_{n+1} P_m - P_n P_{m+1}]$$

so that

$$\tilde{x}_m = \xi A_0 \tilde{V}_m^0 + \sum_{n=-N}^{N} F_n \tilde{V}_m^n + x_{-1} P_m \equiv \kappa_1 P_m + \kappa_2 P_{m+1}.$$

The need for two asymptotic forms of the solution coefficients arises from a basic difference between the current and H_x sums and the E_y and E_z sums, which reflects the difference in the behavior of these terms near the edge of the iris.

A. Current Sums

The current on the iris is simply the difference between the scattered magnetic fields on either side of the iris. Explicitly,

$$J_y = H_x^+ - H_x^- = 2\sin(l\pi x/a) \sum_{m=0}^{\infty} S_{lm} \cos(m\pi y/b)$$

$$= 2\sin(l\pi x/a)[2A_0 + J_s] \qquad (13)$$

where, using the solution coefficient symmetry $x_m = -x_{-m}$, the sum

$$J_s = \sum_{m \neq 0} A_m e^{im\phi}$$

$$= 2 \sum_{m=1}^{\infty} \frac{x_m}{m} \cos m\phi. \qquad (14)$$

This sum is preconditioned by introducing the asymptotic form of the solution coefficients x_m given by (12')

$$J_s = \bar{J}_s + 2 \sum_{m=1}^{\infty} \left(\frac{x_m - \bar{x}_m}{m}\right) \cos m\phi \qquad (15)$$

where the *asymptotic* sum

$$\bar{J}_s = 2 \sum_{m=1}^{\infty} \frac{\bar{x}_m}{m} \cos m\phi \qquad (16)$$

can be handled analytically. It contains the "singular" component of the current near the edge of the iris. As shown in Appendix III, the expression

$$\bar{J}_s(\phi) = -2\kappa_2 \cos\Theta - 2[\kappa_1 + \kappa_2 \cos\phi]$$

$$\cdot \ln\left\{ \sin\frac{\Theta}{2}\left[\cos\frac{\phi}{2} + \left(\cos^2\frac{\phi}{2} - \cos^2\frac{\Theta}{2}\right)^{1/2}\right]\right\}$$

$$+ 2\kappa_2 \sin\phi\left[\sin^{-1}\left(\frac{\sin\frac{\phi}{2}}{\sin\frac{\Theta}{2}}\right) - \phi\right] \qquad (15')$$

is obtained in a straightforward manner. The second sum in (15) converges rapidly numerically and is truncated for $|m| > M$.

B. Electric and Magnetic Field Sums

The electric and magnetic field sums are preconditioned in a similar manner. The resultant expressions for the

components of the total (incident + scattered) fields are

$$H_x = \sin(l\pi x/a)\left\{ S_{lp}^{\mathrm{inc}}\cos(p\pi y/b)e^{-i\gamma_{lp}z}\right.$$

$$+ \mathrm{sgn}(z)\left[2\sum_{m=1}^{\infty}\left(x_m e^{-i\gamma_{lm}|z|} - \bar{x}_m e^{-\zeta_m|z|}\right)\frac{\cos(m\pi y/b)}{m}\right.$$

$$\left.\left. + S_{l0}e^{-i\gamma_{l0}|z|} + Q_x\right]\right\} \tag{17}$$

$$E_y = -\frac{\omega\mu}{k^2 - \left(\dfrac{l\pi}{a}\right)^2}\sin(l\pi x/a)\left\{ \gamma_{lp}S_{lp}^{\mathrm{inc}}\cos(p\pi y/b)e^{-i\gamma_{lp}z}\right.$$

$$+ 2\sum_{m=1}^{\infty}\left(\frac{\gamma_{lm}}{m}x_m e^{-i\gamma_{lm}|z|} + i\frac{\pi}{b}\bar{x}_m e^{-\zeta_m|z|}\right)\cos(m\pi y/b)$$

$$\left. + \gamma_{l0}S_{l0}e^{-i\gamma_{l0}|z|} + Q_y\right\} \tag{18}$$

$$E_z = -\frac{i\omega\mu}{k^2 - \left(\dfrac{l\pi}{a}\right)^2}\sin(l\pi x/a)\left\{ \frac{m\pi}{b}S_{lp}^{\mathrm{inc}}\right.$$

$$\cdot\sin(p\pi y/b)e^{-i\gamma_{lp}z} + \mathrm{sgn}(z)\left[\frac{2\pi}{b}\sum_{m=1}^{\infty}\left(x_m e^{-i\gamma_{lm}|z|}\right.\right.$$

$$\left.\left.\left. - \bar{x}_m e^{-\zeta_m|z|}\right)\sin(m\pi y/b) + Q_z\right]\right\} \tag{19}$$

where $\zeta_m = m\pi/b$. As shown in Appendix IV, setting

$$\alpha = \frac{\pi|z|}{b}$$

$$\lambda_+ = e^{-\alpha}e^{i\phi}$$

$$\lambda_- = e^{-\alpha}e^{-i\phi}$$

so that $|\lambda_+| < 1$ and $|\lambda_-| < 1$ and introducing the terms

$$K(\lambda) = \ln\left(\frac{2}{1 - \lambda\cos\Theta + \sqrt{1 - 2\lambda\cos\Theta + \lambda^2}}\right) \tag{20}$$

$$L(\lambda) = \frac{\kappa_1 + \lambda^{-1}\kappa_2}{\sqrt{1 - 2\lambda\cos\Theta + \lambda^2}} \tag{21}$$

the analytically calculated sums are

$$Q_x = \left(\kappa_1 + \lambda_+^{-1}\kappa_2\right)K(\lambda_+)$$

$$+ \left(\kappa_1 + \lambda_-^{-1}\kappa_2\right)K(\lambda_-) - 2\kappa_2\cos\Theta \tag{22a}$$

$$Q_y = -\frac{i\pi}{b}\left\{ L(\lambda_+) + L(\lambda_-)\right.$$

$$\left. - 2\left[\kappa_1 + \kappa_2(\cos\Theta + e^\alpha\cos\phi)\right]\right\} \tag{22b}$$

$$Q_z = -\frac{i\pi}{b}\left[L(\lambda_+) - L(\lambda_-) + 2i\kappa_2 e^\alpha\sin\phi\right]. \tag{22c}$$

Note that for $z = 0$, the factors $\lambda_+ = e^{i\phi}$ and $\lambda_- = e^{-i\phi}$; thus, near the edge of the iris, where $\phi \sim \Theta - \epsilon$, giving

$\cos\phi \sim \cos\Theta + \epsilon\cos\Theta$, the field terms

$$\left(1 - 2\lambda_+\cos\Theta + \lambda_+^2\right)^{-1/2}$$

$$= e^{-i\phi/2}\left[2(\cos\phi - \cos\Theta)\right]^{-1/2} \sim \epsilon^{-1/2}$$

$$\left(1 - 2\lambda_-\cos\Theta + \lambda_-^2\right)^{-1/2}$$

$$= e^{+i\phi/2}\left[2(\cos\phi - \cos\Theta)\right]^{-1/2} \sim \epsilon^{-1/2}.$$

This demonstrates that the square root singularity of the transverse electric field components E_y and E_z near the iris edge have been isolated in the Q_y and Q_z expressions and, hence, are treated analytically. The summations in (17)–(19) are handled numerically without difficulty and converge rapidly.

IV. SAMPLE RESULTS

A large number of results for the capacitive iris case have been generated with the dual-series solution. Representative examples will be presented below that illustrate the basic phenomena we have observed. Unless otherwise indicated, all results pertain to a WR-284 waveguide (7.21 cm by 3.40 cm) and were obtained with the truncation parameters $N = 50$ and $M = 200$. These truncation parameter values were chosen to guarantee convergence of the results in all of the given cases. Note that the cutoff frequencies associated with this particular waveguide that are of interest here are $(f_c)_{10} = 2.082$ GHz, $(f_c)_{11} = 4.876$ GHz, $(f_c)_{12} = 9.060$ GHz, $(f_c)_{13} = 13.389$ GHz, $(f_c)_{20} = 4.164$ GHz, $(f_c)_{21} = 6.064$ GHz, $(f_c)_{22} = 9.751$ GHz, and $(f_c)_{23} = 13.866$ GHz. Also note that in the vector plots discussed below, the vectors drawn depict both the relative magnitude (the largest vector length is selected proportional to the largest magnitude) and direction of the quantity under scrutiny.

The currents established on the iris provide a definitive check on the satisfaction of Meixner's edge conditions by the generalized dual-series solution. The real (solid lines) and imaginary (dashed lines) parts of the current induced on a 75-percent iris by a TE_{10} mode of frequency at 3, 8, 11, and 15 GHz are shown in Fig. 2. The corresponding magnitude plots are given in Fig. 3(a)–(d). The requisite "square-root to zero" behavior of the currents at the iris edge is readily discernible. The number of peaks in Fig. 3(a)–(d) is correlated to the number of propagating scattered modes. At 3 GHz, there is only the fundamental mode present. At 8 and 11 GHz, the guide supports two propagating modes. At 15 GHz, there are three propagating modes present.

Fig. 4 illustrates the efficacy of our field calculations near the edge of the iris. Contours of the electric field are given respectively for a 3-GHz and a 4-GHz excitation. The large values of the contours correspond to the presence of a singularity in the field at the edge of the iris.

The interplay of the incident wave and the modes scattered from the iris proved to be more interesting than first expected. As demonstrated in Figs. 5–8 for a TE_{10} wave incident upon a 50-percent iris configuration, the
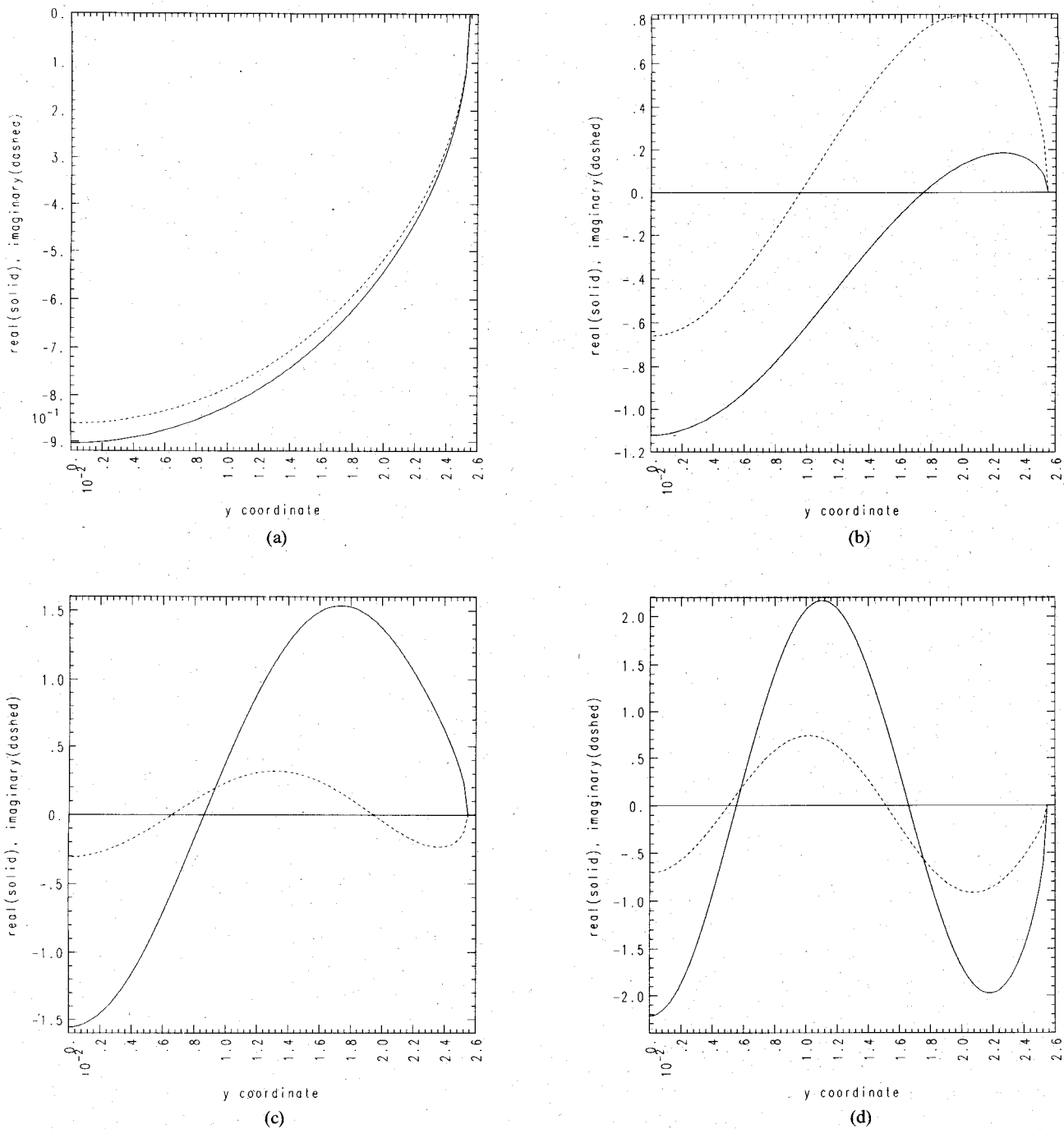
Fig. 2. Real (solid lines) and imaginary (dashed lines) parts of the current induced on a 75-percent iris by a TE_{10} mode incident at frequencies of (a) 3 GHz, (b) 8 GHz, (c) 11 GHz, and (d) 15 GHz.

onset of the higher order, propagating scattered modes leads to the creation of vortices. The higher order modes provide the transverse power flow required for the vortex formation. The vortices appear in a periodic manner for both the regions $z < 0$ and $z > 0$. However, in comparison to the region $z > 0$, the overall pattern of the vortices for $z < 0$ is more complex due to the reflection of the incident wave from the iris.

To illustrate these effects, consider, for example, the onset of the second propagating mode at 4.87 GHz. Fig. 5(a)–(d) represent the response to 4.70-GHz, 4.85-GHz,

4.95-GHz, and 5.10-GHz excitations, respectively. Vector plots of the real part of the Poynting vector $\vec{P}$ and the corresponding contour plots are given for each frequency. Notice in Fig. 5(b) that just prior to the TE_{12} mode threshold, the power pattern is very symmetrical about the iris while just past this threshold it is very asymmetrical. Completely formed vortices are represented by nulls in the power pattern resulting from corresponding nulls in the magnetic field. The contour boundaries were generated using linear interpolation of values on a rectilinear grid. The sharp corners that are apparent in some of the contour
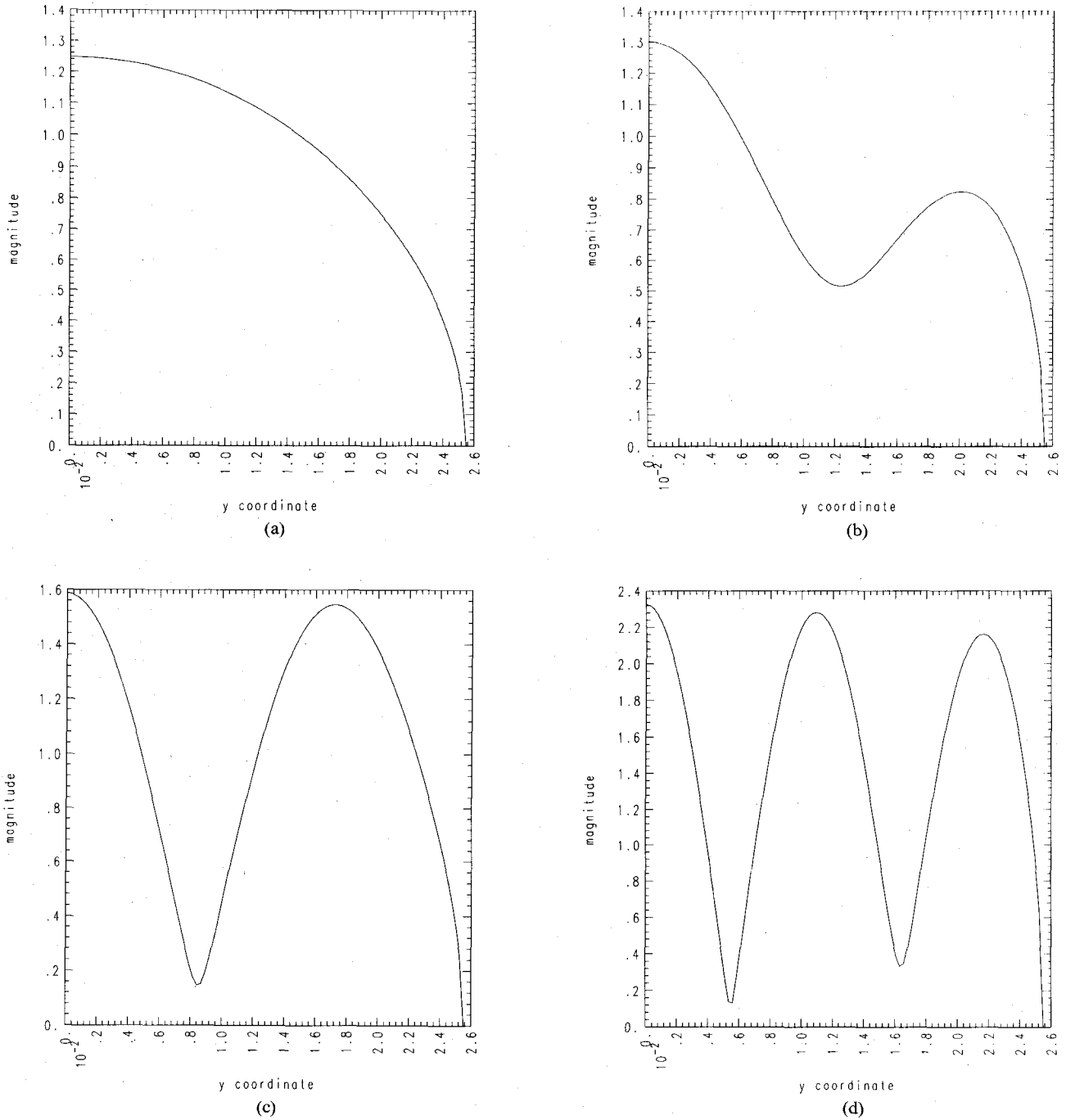
Fig. 3. Magnitudes of the current induced on a 75-percent iris by a TE_{10} mode incident at the frequencies (a) 3 GHz, (b) 8 GHz, (c) 11 GHz, and (d) 15 GHz.
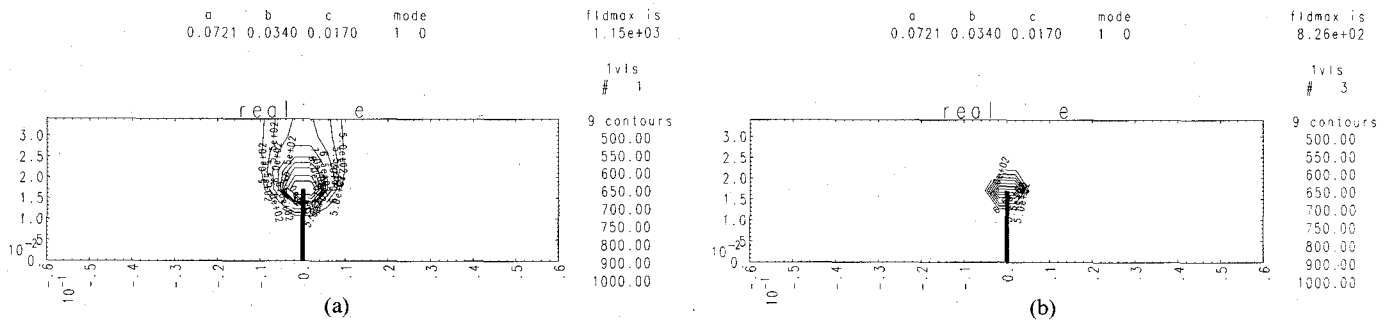

Fig. 4. The presence of the edge singularity is observed in the contour plots of the real part of the electric field for a 50-percent iris and a TE_{10} mode incident at the frequencies (a) 3.0 GHz and (b) 4.0 GHz.
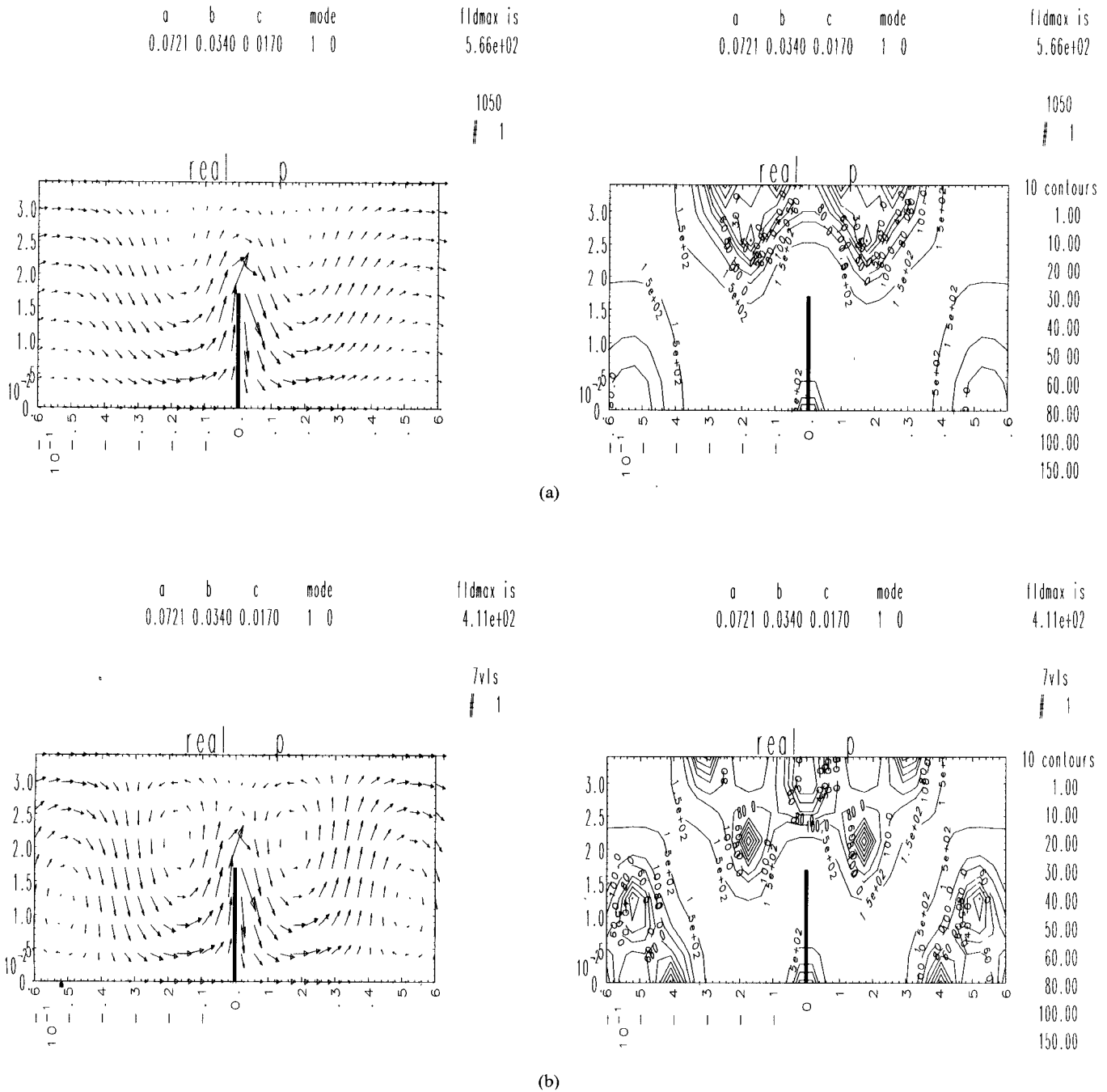
(a)

(b)

Fig. 5. The formation of vortices in the iris region after the onset of higher order scattered modes is illustrated with vector and contour plots of Re $\vec{P}$ for a 50-percent iris and a TE_{10} mode incident at the frequencies (a) 4.70 GHz, (b) 4.85 GHz.

plots are an artifact of this process and occur when variations exist that are smaller than the grid spacing.

As illustrated in Fig. 6(a)–(c), where vector and contour plots of Re $\vec{P}$ and contour plots of $|H_x|$ are given for incident frequencies of 3.0 GHz (top plot), 5.0 GHz (middle plot), and 9.1 GHz (bottom plot), the number of vortices present is directly connected to the number of propagating modes scattered by the iris. Furthermore, as shown in Fig. 6(a), the evanescent modes scattered from the iris are responsible for "lifting" the power flow over the iris. Without their presence, the power would simply

flow longitudinally along the length of the waveguide. Note, however, that as the frequency increases, the domain of influence of the evanescent modes becomes more localized to the vicinity of the iris, thus diminishing their role in the field patterns or power flow. Consequently, the vortex formation is found to be purely a consequence of the interplay of the propagating modes.

The view of the 5.0-GHz case is expanded in Fig. 7(a) and (b) to demonstrate the periodic location of the vortices. The vector plot of Re $\vec{P}$ and the contour plot of $|H_x|$ are given in Fig. 7(a) for -13.0 cm $\leqslant z \leqslant 0.1$ cm and in Fig.
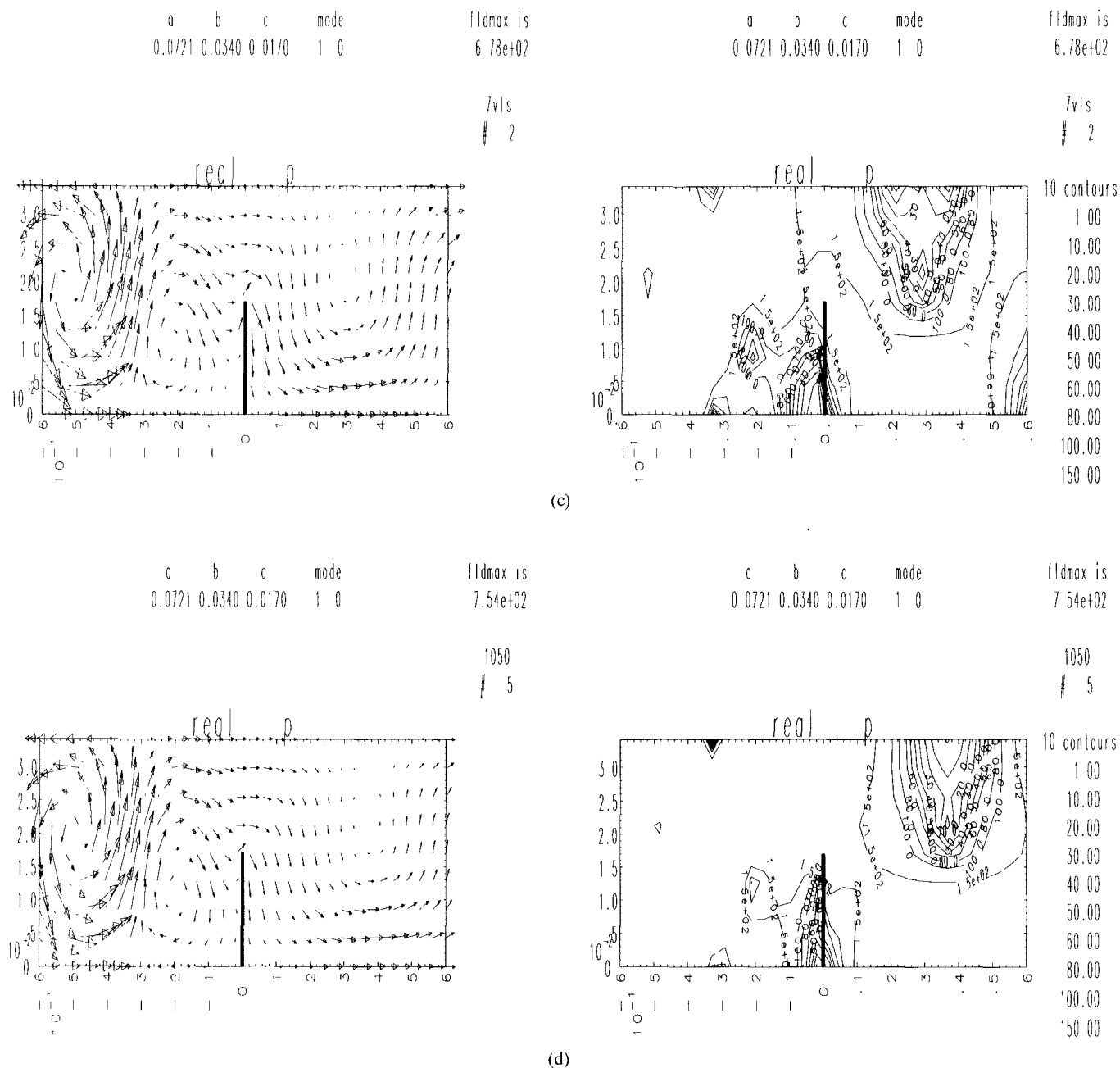
a   b   c   mode |ldmax is
0.0721 0.0340 0.0170   1 0   6.78e+02

a   b   c   mode |ldmax is
0.0721 0.0340 0.0170   1 0   6.78e+02

|v|s
2

|v|s
2

real   p

real   p

10 contours
1.00
10.00
20.00
30.00
40.00
50.00
60.00
80.00
100.00
150.00

(c)

a   b   c   mode |ldmax is
0.0721 0.0340 0.0170   1 0   7.54e+02

a   b   c   mode |ldmax is
0.0721 0.0340 0.0170   1 0   7.54e+02

1050
5

1050
5

real   p

real   p

10 contours
1.00
10.00
20.00
30.00
40.00
50.00
60.00
80.00
100.00
150.00

(d)

Fig. 5. (cont.)   (c) 4.95 GHz and (d) 5.10 GHz.

7(b) for -0.1 cm $\leq z \leq 13.0$ cm. Because a vortex arises solely from the superposition of the propagating modes, its location in z depends only on the phase difference between the propagation factors and the phases of the modal coefficients associated with those modes. Thus, the vortex locations appear periodically in z relative to the vortex nearest the iris. Behind the iris, an increase in frequency causes the location of the first vortex and, hence, all the other vortices to move in tandem away from the iris. This apparent movement of the vortex centers behind the iris creates the effect shown in Fig. 8, where contours of $|H_x|$ are given for incident frequencies of a) 5.0 GHz, b) 6.5 GHz, c) 7.5 GHz, and d) 9.0 GHz. The iris appears to be shedding vortices with increasing frequency. On the other hand, for $z < 0$, as the frequency increases, the additional

interaction of the reflected wave with the incident and propagating higher order scattered waves causes a breakup of the larger vortices present at the lower frequencies into clusters of smaller ones at the higher frequencies. Moreover, after the appearance of the second propagating mode, there is always a well-defined vortex located directly in front of the iris. Its location actually slightly approaches the iris as the frequency is increased. The other vortices in this region are then periodically located relative to this vortex.

The vortices appear even for small irises, as shown in Fig. 9, where vector plots of $\vec{P}$ are given for a 30-percent iris and for incident fields of frequencies 3.0 GHz and 9.5 GHz. As demonstrated in Fig. 10(a) and (b) for a 6.0-GHz TE_{10} wave incident, respectively, on a 50-percent and a
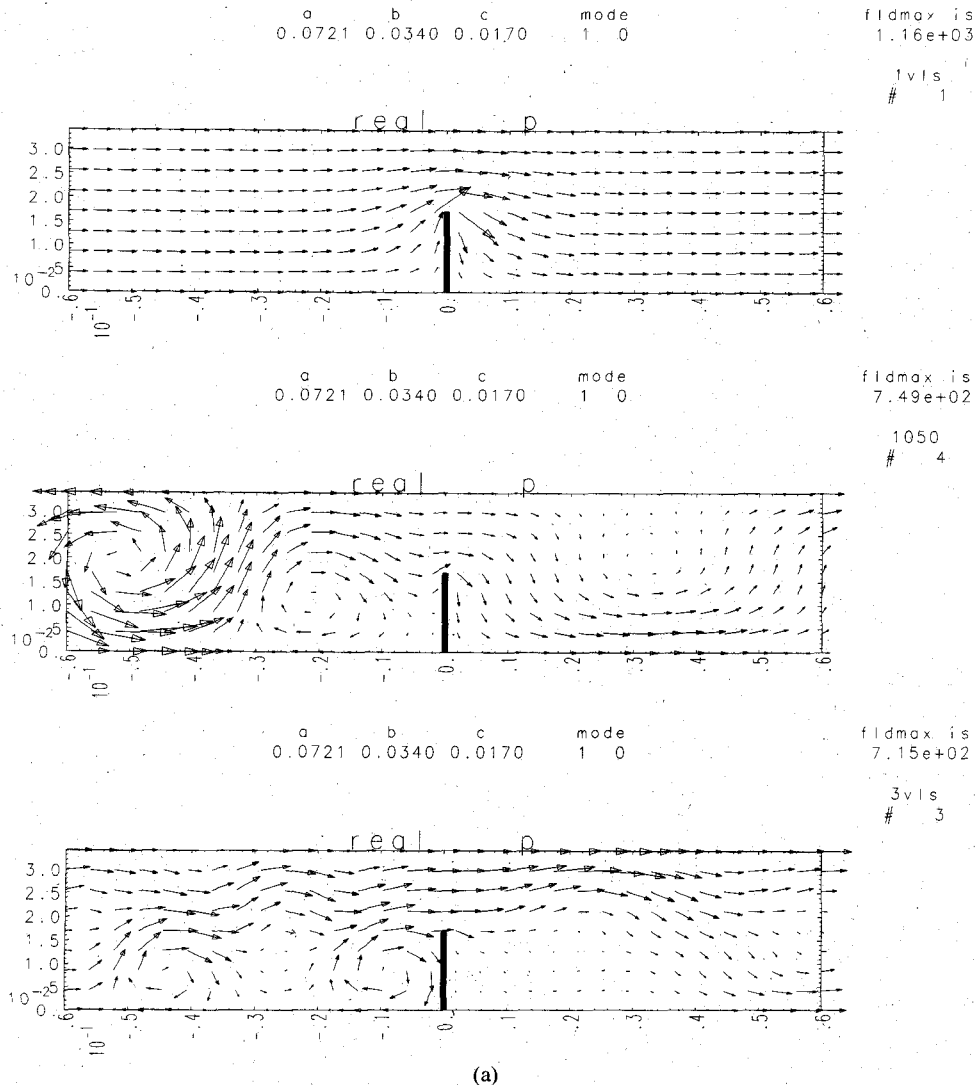
Fig. 6. As the number of higher order scattered modes increases, the number of vortices increases. This is illustrated with (a) vector plots of $\mathrm{Re}\,\vec{P}$ for a 50-percent iris and a TE_{10} mode incident at frequencies of 3.0 GHz (top), 5.0 GHz (middle), and 9.1 GHz (bottom).

70-percent iris, the vortex directly in front of the iris matches its height to the height of the iris. This appears necessary to channel the power flow above the iris. As is apparent in all of the above cases, when vortex formation occurs, the power flow along the guide can be drastically altered from the uniform flow found in an empty guide. To emphasize this point, the small (middle) and large (bottom) power contours are included in Fig. 11 along with the vector plot (top) of the 70-percent iris case given in Fig. 10(b). One turbulent vortex and several weaker vortices have been established that create a very nonuniform channeling of the power flow in the vicinity of the iris.

Because their structure is more complicated, more complex vortex patterns occur when higher order modes are incident upon the iris. This is demonstrated in Fig. 12(a)–(d) for an 8.0-GHz signal. A TE_{11} mode is incident, respectively, upon a 50-percent and a 70-percent iris in Fig. 12(a) and (c). A TE_{20} mode is incident upon the same irises in Fig. 12(b) and (d). In contrast to the TE_{10} mode

incidence case, the TE_{11} mode pattern creates several more smaller vortices directly in front of the iris. The TE_{20} cases are very much the same as for the TE_{10} mode except that the vortices appear at different frequencies due to the different cutoff frequencies of the TE_{2m} modes.

Since the frequency scans discussed above can be extended to a much finer scale, one can construct the transfer function for the capacitive waveguide iris configuration. Then, using an FFT algorithm, time-domain field configurations can be made. We have actually made movies for a limited number of cases involving narrow-band, pulsed excitations. As one would expect, these time-domain results mimicked frequency-domain results for the carrier frequency. Vortex formation was apparent as the pulse interacted with the iris.

V. SUMMARY

The generalized dual-series solutions to the capacitive and inductive waveguide iris problems were presented.
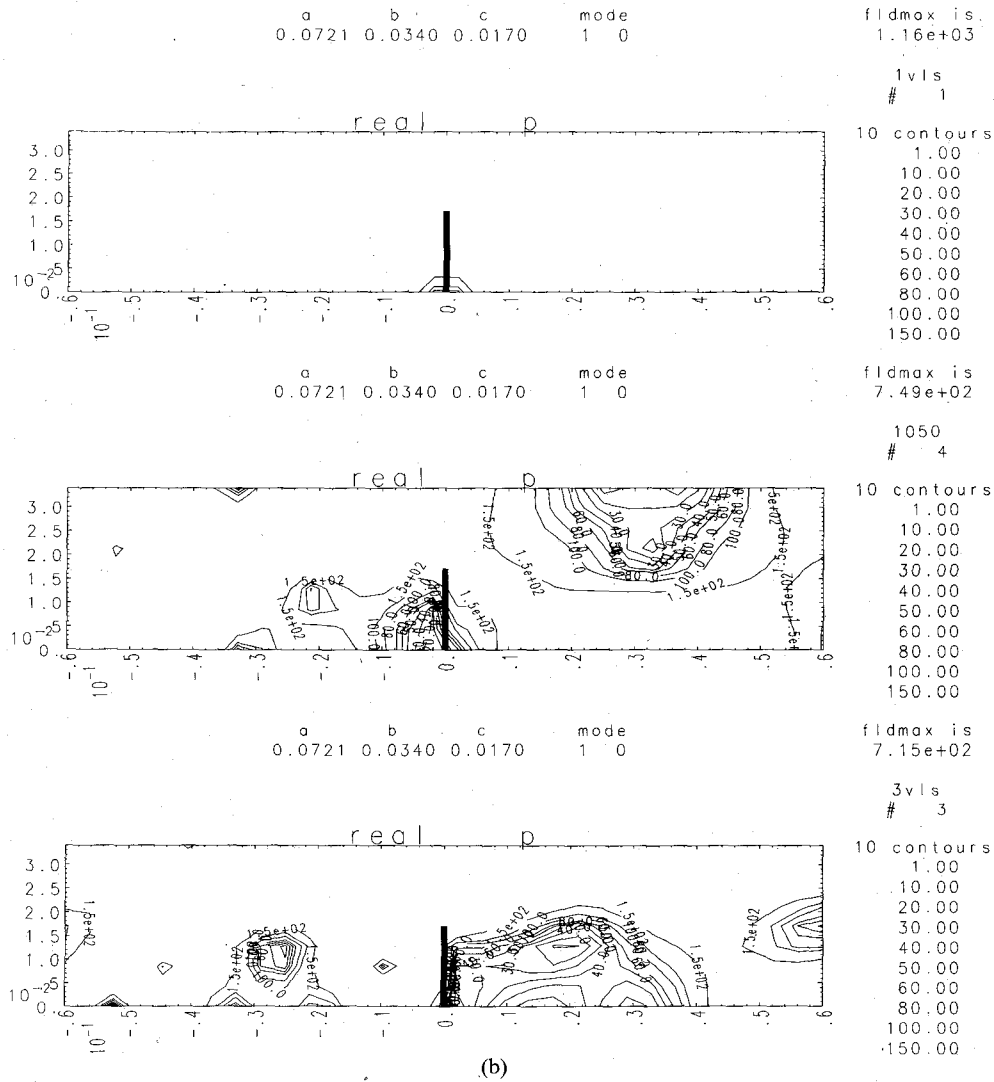
Fig. 6. (cont.) (b) Contour plots of Re $\vec{P}$.

Numerical results were given only for the capacitive iris case. They were used to investigate the formation of vortices near the iris and the effect these vortices had on the local field configurations there.

This study actually originated with the desire to analyze the local field enhancements near the edge of the iris for gas breakdown studies in progress at our laboratory. In addition to enhancements near the iris, our studies have demonstrated that the local "hotspots" created by the vortex formation may have significant roles in that experimental work. Moreover, the vortices themselves may play an important part in the transport or trapping of the breakdown plasma in the vicinity of the iris.

With regard to experimental verification, vortices have been observed by Liska and Meinke in rectangular waveguides having step discontinuities [31]. Meinke and his coworkers also investigated the use of energy flow diagrams to describe the operation of a variety of microwave devices and antennas in the 1970's. Energy flow diagrams for the step discontinuity measured in [31] appear in [32].

APPENDIX I
RIEMANN-HILBERT PROBLEMS

The Reimann–Hilbert problem is a classical problem in complex variable theory. It concerns the construction of the analytic function x whose limits x_+ and x_- from the inside and the outside of a closed curve satisfy the transition condition $x_- = gx_+ + h$ on an open segment of that curve. Consider first the "capacitive" dual-series system (9), which is repeated here for convenience

$$\sum_{m=-\infty}^{\infty} A_m e^{im\phi} = 0 \qquad (|\phi| > \Theta) \qquad (9a)$$

$$\sum_{m=-\infty}^{\infty} A_m |m| (1 + \chi_m) e^{im\phi} = f(\phi) \qquad (|\phi| < \Theta). \qquad (9b)$$

Recall that (9a) and (9b) are associated with, respectively, the field components H_x and E_y. Therefore, they behave, respectively, like $(\Theta - \phi)^{1/2}$ and $(\Theta - \phi)^{-1/2}$ near the edge of the iris. To make both series equations display the same singular behavior, (9a) is differentiated with respect to ϕ. Introducing the coefficients $x_m = mA_m$ (note that it is
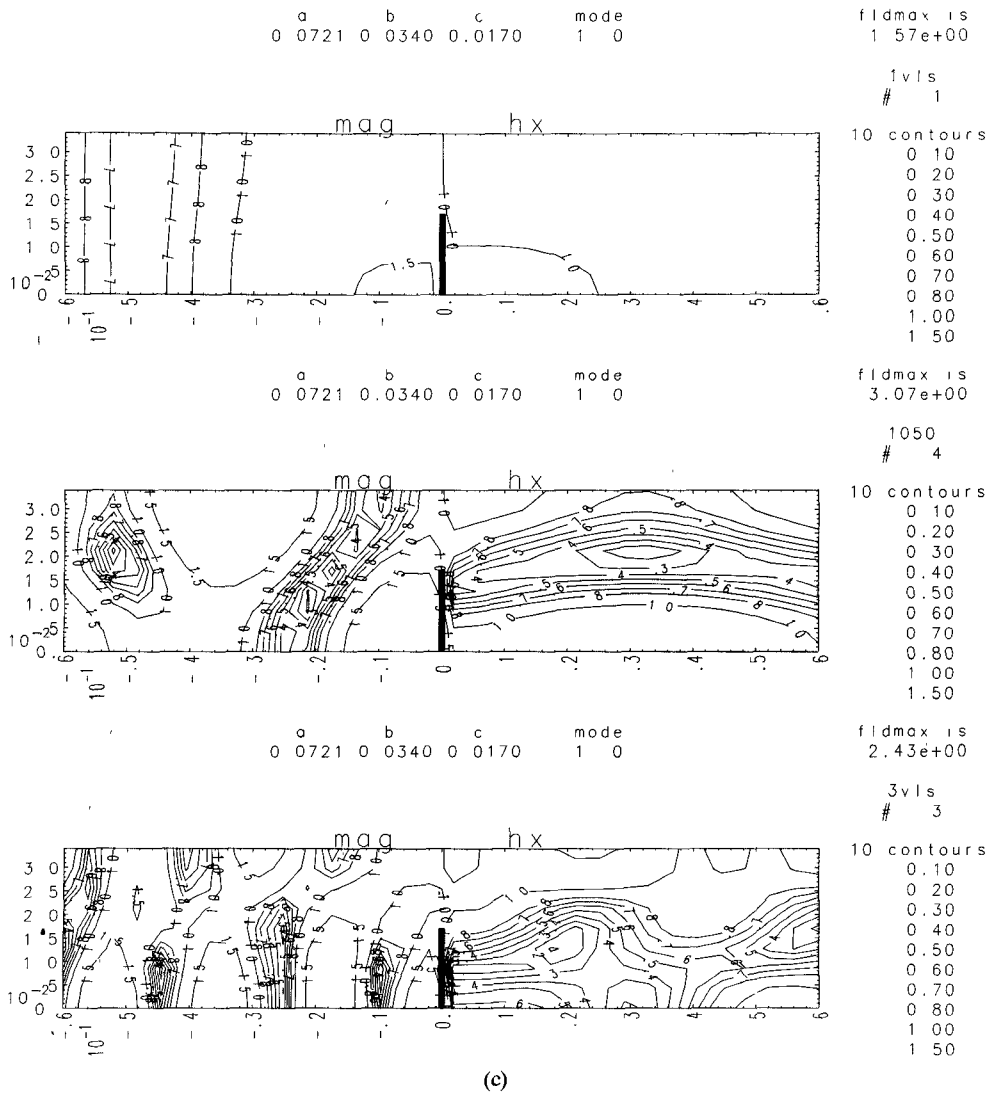
Fig. 6. (cont.) (c) Contour plots of $|H_x|$.

assumed that $x_0 \equiv 0$ and the functions

$$x_+(z) = \sum_{m>0} x_m z^m$$

$$x_-(z) = \sum_{m<0} x_m z^{-m}$$

$$F(z) = \xi A_0 + \sum_{m=-\infty}^{\infty} \left(f_m - x_m \frac{|m|}{m} \chi_m \right) z^m$$

the dual series (9) can then be written simply as

$$x_+(e^{i\phi}) - x_-(e^{i\phi}) = 0 \qquad (|\phi| > \Theta) \quad \text{(A1a)}$$

$$x_+(e^{i\phi}) + x_-(e^{i\phi}) = F(e^{i\phi}) \qquad (|\phi| < \Theta). \quad \text{(A1b)}$$

This system represents the equivalent Riemann–Hilbert problem. Equation (A1a) reflects the continuity of the magnetic field across the aperture; equation (A1b), the transition condition the electric field must satisfy across the iris. As explained in [22], its solution is the Fredholm equation of the second kind

$$x_m = \xi A_0 V_m^0 + \sum_{n=-\infty}^{\infty} \left(f_n - \frac{|n|}{n} \chi_n x_n \right) V_m^n + x_{-1} P_m \quad \text{(A2)}$$

where $(m = 0, \pm 1, \pm 2, \cdots)$. This infinite linear system is completed with the auxiliary condition

$$A_0 = - \sum_{m \neq 0} \frac{(-)^m}{m} x_m \quad \text{(A3)}$$

which is obtained from (9a) with $\phi = \pi$; it is introduced to account for the constant eliminated in the differentiation that led from (9a) to (A1a). This constraint leads to the expression

$$-A_0 = \xi A_0 W^0 + \sum_{n=-\infty}^{\infty} \left(f_n - \frac{|n|}{n} \chi_n x_n \right) W^n - 2S x_{-1}$$
$$\text{(A4)}$$

where

$$W^n = \sum_{m \neq 0} \frac{(-)^m}{m} V_m^n \quad \text{and} \quad S = \frac{1}{2} \sum_{m \neq 0} \frac{(-)^m}{m} P_m.$$

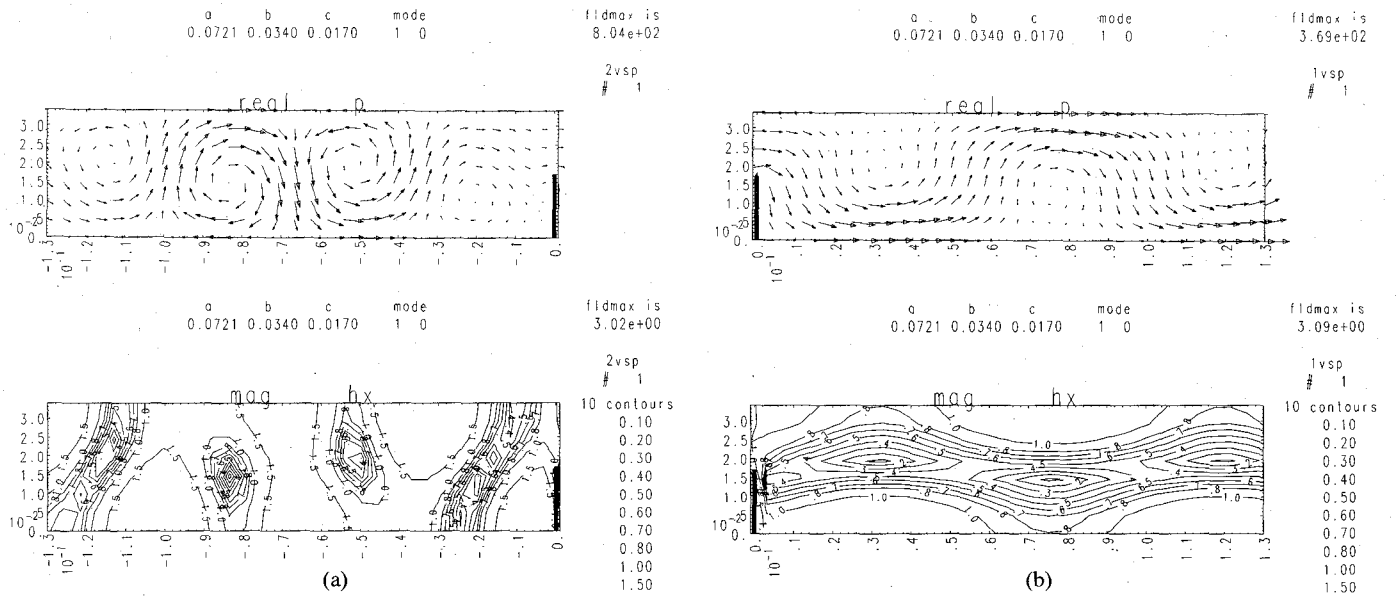Equations (A2) and (A4) uniquely define the desired modal coefficients.

Fig. 7. The periodicity in the location of the vortices is illustrated with an increase in the field of view to (a) -13.0 cm $\leqslant z \leqslant 0.1$ cm and (b) -0.1 cm $\leqslant z \leqslant 13.0$ cm of the 5.0-GHz, 50-percent iris case vector plot of Re $\vec{P}$ and contour plot of $|H_x|$ given in Fig. 6.
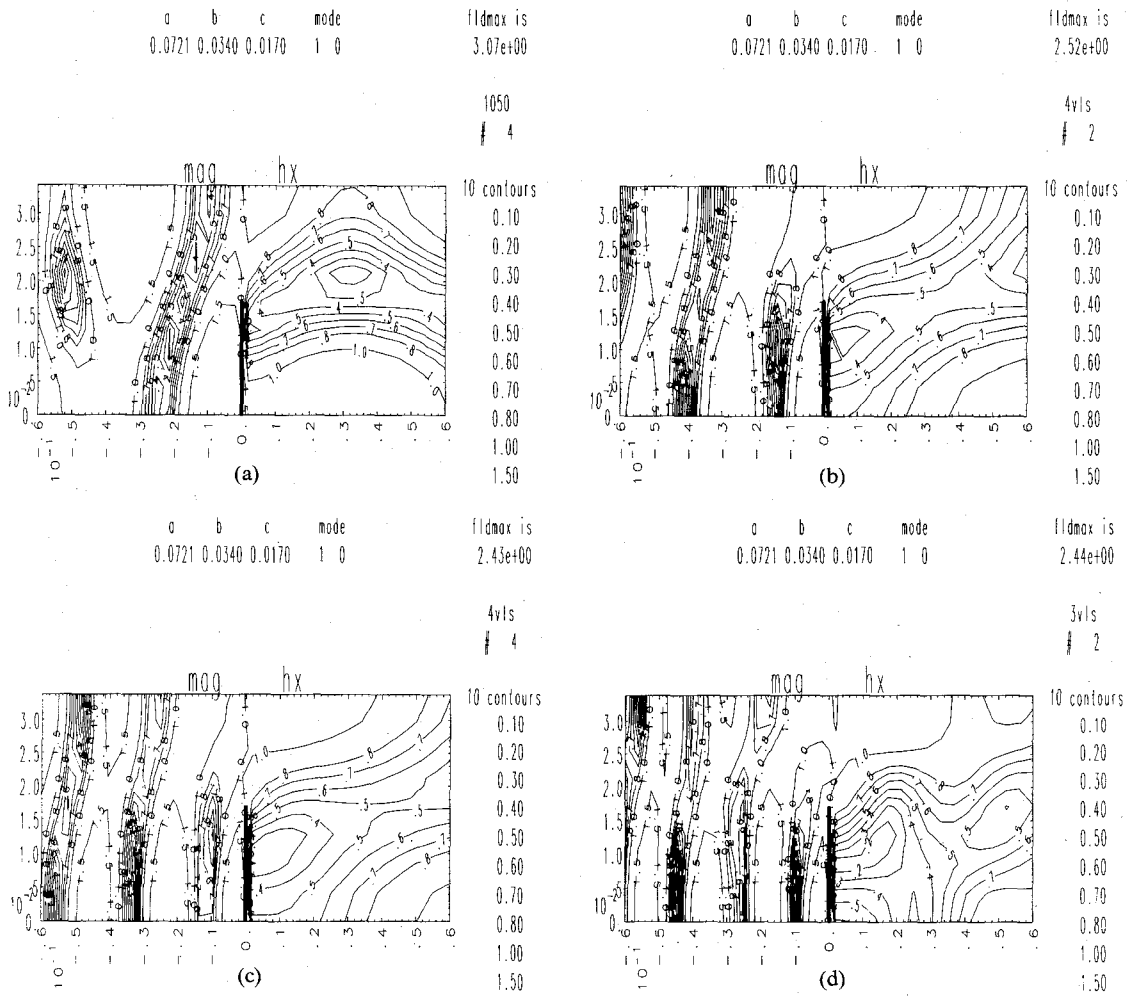

Fig. 8. The iris appears to shed vortices as the frequency increases, as shown by these contour plots of $|H_x|$ for a 50-percent iris and a TE_{10} mode incident at frequencies of (a) 5.0 GHz, (b) 6.5 GHz, (c) 7.5 GHz, and (d) 9.0 GHz.
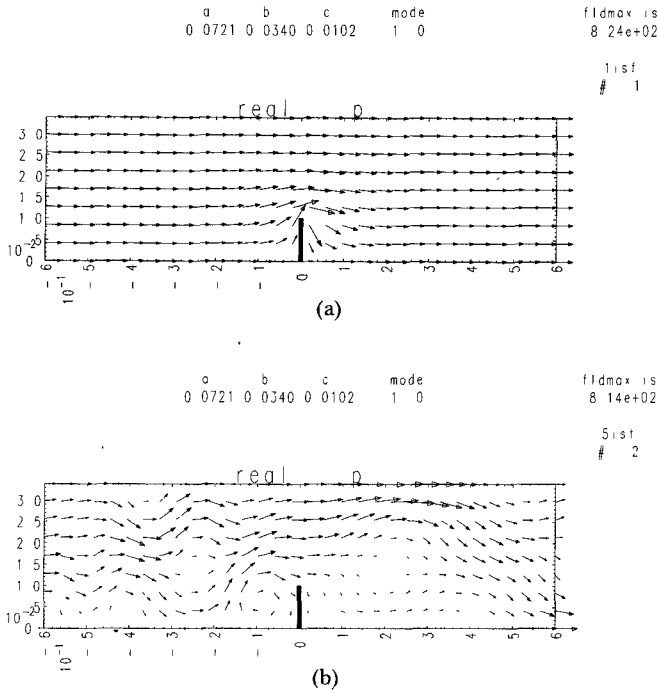
Fig. 9. Vector plots of Re $\vec{P}$ for a 30-percent iris and a TE_{10} mode incident at frequencies of (a) 3.0 GHz and (b) 9.5 GHz indicate that the vortex behavior for a short iris is qualitatively the same as for a taller iris.

Fig. 10. Vector plots of Re $\vec{P}$ for a 6.0-GHz, TE_{10} mode scattered from a (a) 50-percent and (b) a 70-percent iris show that the vortices directly in front of the iris match their height to the height of the iris.

Now consider the inductive iris dual-series system

$$\sum_{m=0}^{\infty} \gamma_{lm} T_{lm} \sin(m\pi y/b) = 0 \qquad (c < y \leqslant b) \qquad (2a)$$

$$\sum_{m=0}^{\infty} T_{lm} \sin(m\pi y/b) = -T_{lp}^{\text{inc}} \sin(p\pi y/b)$$

$$(0 \leqslant y < c). \qquad (2b)$$

It differs from the capacitive iris case by the presence of the γ_{lm} term now in the aperture relation (2a). Recalling that (2b) and (2a) are associated with, respectively, the field components E_x and H_y, they behave like $(\Theta - \phi)^{1/2}$ and $(\Theta - \phi)^{-1/2}$ near the edge of the iris. As in the capacitive iris case, the γ_{lm} term is responsible for this difference. Nonetheless, the dual-series system (2) can be reduced to the form (A1) as follows. Let the angles $\psi = \pi - \phi$ and $\Psi = \pi - \Theta$ and the coefficients

$$\tilde{T}_{lm} = T_{lm} + T_{lp}^{\text{inc}}\delta_{mp} \quad \text{and} \quad B_m = \frac{1}{2}\,\text{sgn}(m)\tilde{T}_{l|m|} \quad \text{and}$$

$$g_m = \frac{\text{sgn}(m)}{2}\tau_m T_{l|m|}^{\text{inc}}\delta_{mp}.$$

Differentiating (2a), one then obtains

$$\sum_{m \neq 0} B_m \tau_m e^{im\psi} = \sum_{m \neq 0} g_m e^{im\psi} \qquad (|\psi| < \Psi)$$

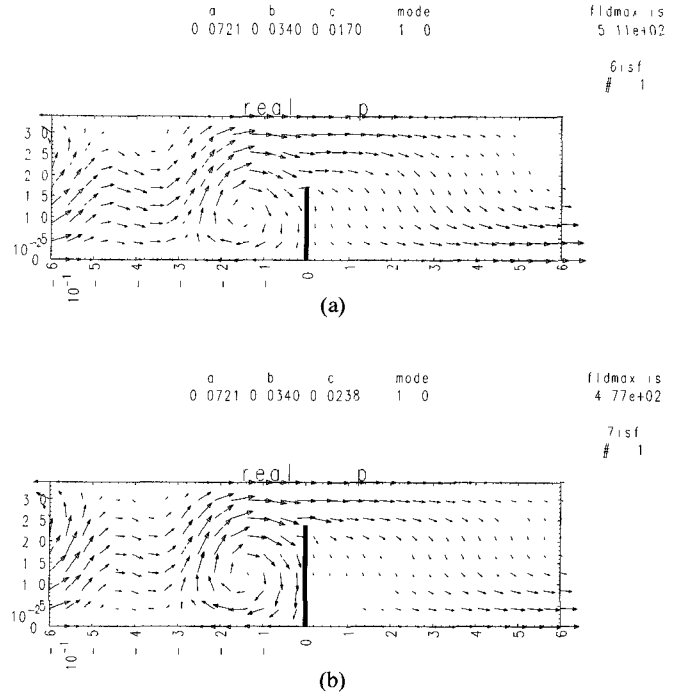$$\sum_{m \neq 0} m B_m e^{im\psi} = 0 \qquad (|\psi| > \Psi).$$

Finally, set

$$y_m = \text{sgn}(m) m B_m \quad \text{and}$$

$$G(z) = \sum_{m \neq 0} \left(g_m - \frac{|m|}{m} \chi_m y_m \right) z^m.$$

With the definitions of $y_+(z)$ and $y_-(z)$ the same as in the capacitive case except, of course, for y_m replacing x_m, this dual-series system takes the Riemann–Hilbert problem form

$$y_+(e^{i\psi}) - y_-(e^{i\psi}) = 0 \qquad (|\psi| > \Psi) \qquad (A5a)$$

$$y_+(e^{i\psi}) + y_-(e^{i\psi}) = G(e^{i\psi}) \qquad (|\psi| < \Psi). \qquad (A5b)$$

The desired solution then is simply

$$y_m = \sum_{n \neq 0} \left(g_n - \frac{|n|}{n} \chi_n y_n \right) V_m^n + y_{-1} P_m. \qquad (A6)$$

Since there was no constant lost in the differentiation of (2a), no auxiliary conditions are required here and (A6) uniquely defines the inductive iris solution.

Note that a formal solution of a Riemann–Hilbert problem involving singularities of the type $r^{-\alpha}$, where $0 < \alpha < 1$, exists [22]. The thin-iris problems naturally embody the $r^{-1/2}$ case. The particular form of (A1) and (A5) reflect this property.

APPENDIX II
COEFFICIENT DEFINITIONS

The inversion coefficients V_m^n for $m \neq n$ are given by the expression

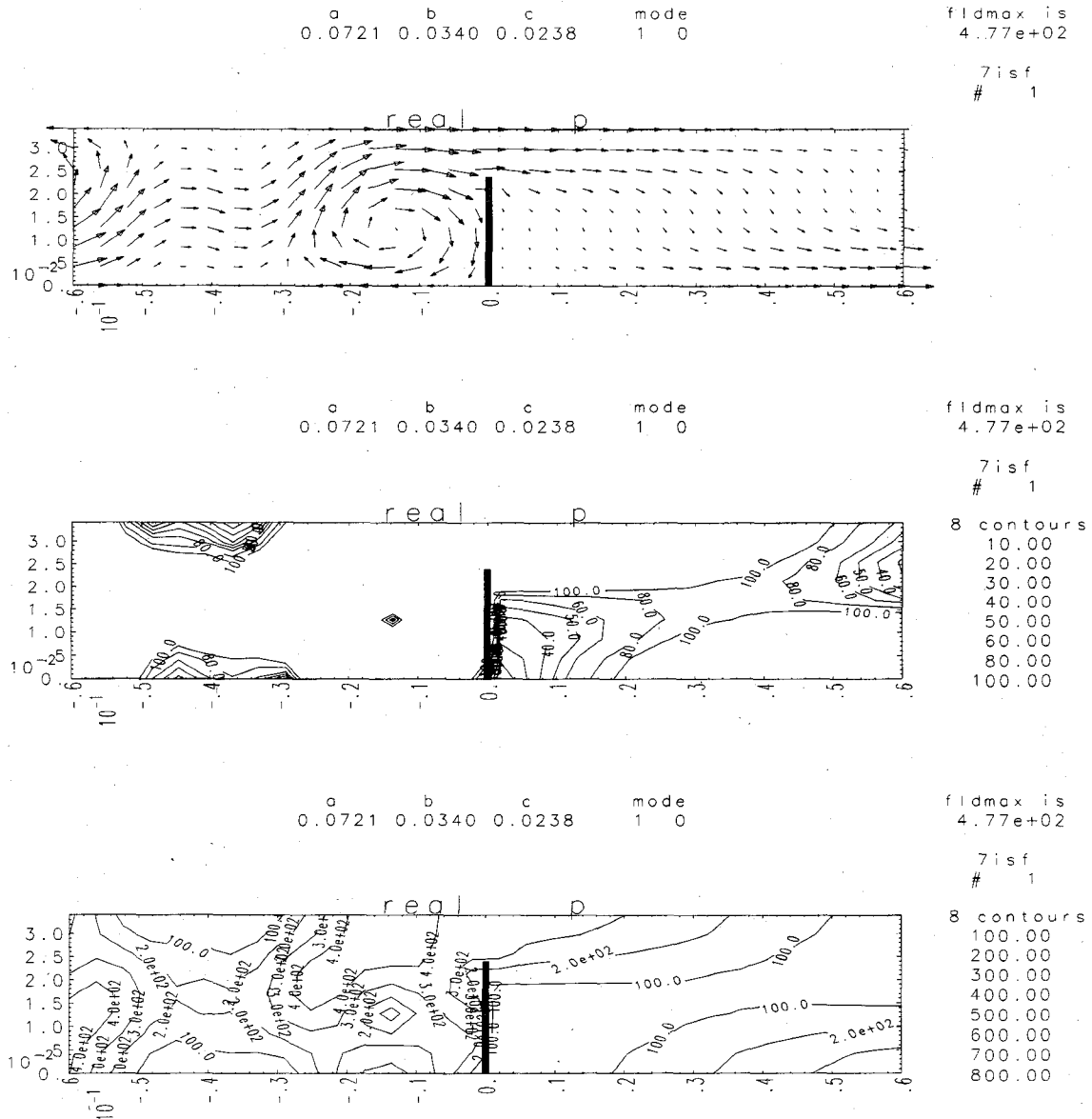$$V_m^n = \frac{m+1}{2(m-n)} \left[P_m(u) P_{n+1}(u) - P_{m+1}(u) P_n(u) \right].$$

Fig. 11.   Vector plots and contour plots of Re $\vec{P}$ for a TE_{10} mode incident at 6.0 GHz on a 70-percent iris show the power strongly channeled by the vortices.

The special case when $m = n$ is given by

$$V_n^n = \frac{n+1}{2} \left[U_n(u) P_{n+1}(u) - U_{n+1}(u) P_n(u) \right]$$

where

$$U_0(u) = 0$$

$$U_1(u) = u - 1$$

$$U_{n+1}(u) = \frac{u P_n(u) - P_{n-1}(u)}{(n+1)^2} + \frac{2n+1}{n+1} u U_n(u)$$

$$- \frac{n}{n+1} U_{n-1}(u)$$

and

$$P_{-n}(u) = P_{n-1}(u)$$

$$U_{-n}(u) = U_{n-1}(u).$$

The remaining coefficient terms are defined as

$$W^n = -\frac{1}{2} \mu_{n+1}(u) \ln\left(\frac{1+u}{2}\right) + \frac{1}{2n} \left[P_n(u) - P_{n-1}(u) \right]$$

$$R_m = \frac{1}{2} P_m(u)$$

$$S = \sum_{m \neq 0} (-)^m \frac{R_m(u)}{m} = -\frac{1}{2} \ln\left(\frac{1+u}{2}\right)$$

where

$$u = \cos(\Theta)$$

and

$$\mu_0(u) = 1$$

$$\mu_1(u) = -P_1(u) = -u$$

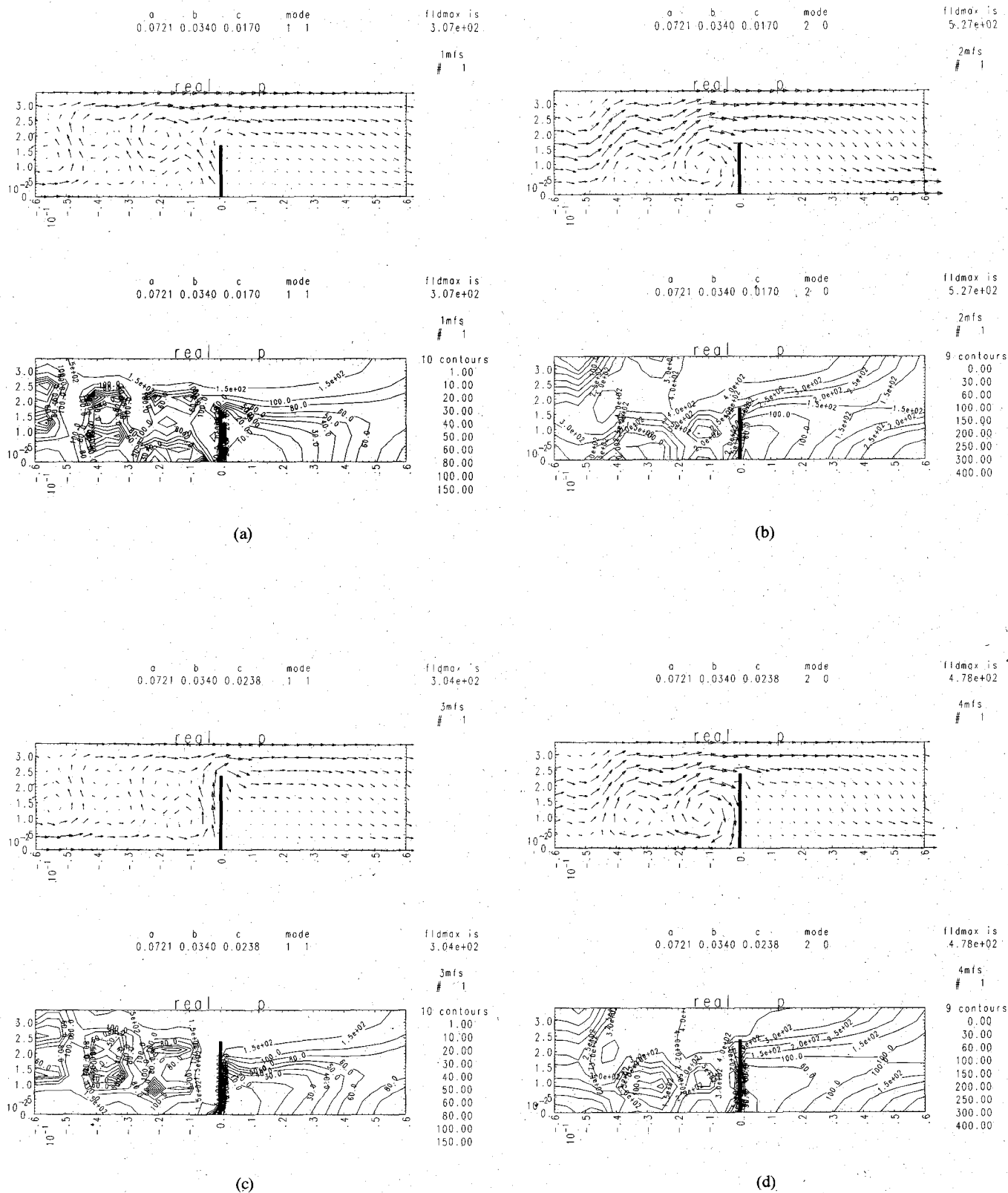$$\mu_n(u) = P_n(u) - 2u P_{n-1}(u) + P_{n-2}(u) \qquad \text{for } (n \geq 2).$$

Fig. 12. The generalized dual-series solution can also model the incidence of higher order modes. Vector and contour plots of Re $\vec{P}$ are given at 8.0 GHz for (a) a TE_{11} mode incident on a 50-percent iris, (b) a TE_{20} mode incident on a 50-percent iris, (c) a TE_{11} mode incident on a 70-percent iris, and (d) a TE_{20} mode incident on a 70-percent iris.

APPENDIX III
CURRENT SUM FORMULA

The current sum formula (15′) follows from the summation formula [33]

$$\sum_{m=0}^{\infty} P_m(\cos\Theta)\sin m\phi$$

$$= \begin{cases} -\sin\dfrac{\phi}{2}\left[2(\cos\phi-\cos\Theta)\right]^{-1/2} & (\phi<\Theta) \\[2ex] -\cos\dfrac{\phi}{2}\left[2(\cos\Theta-\cos\phi)\right]^{-1/2} & (\phi>\Theta) \end{cases} \quad (A7)$$

$$\sum_{m=0}^{\infty} P_m(\cos\Theta)\cos m\phi$$

$$= \begin{cases} +\cos\dfrac{\phi}{2}\left[2(\cos\phi-\cos\Theta)\right]^{-1/2} & (\phi<\Theta) \\[2ex] -\sin\dfrac{\phi}{2}\left[2(\cos\Theta-\cos\phi)\right]^{-1/2} & (\phi>\Theta) \end{cases} \quad (A8)$$

and from the integrals

$$I_1 = \int_0^{\phi} \frac{\sin\dfrac{\phi}{2}\, d\phi}{\left[2(\cos\phi-\cos\Theta)\right]^{1/2}}$$

$$= -\ln\left[\frac{\cos\dfrac{\phi}{2}+\left(\cos^2\dfrac{\phi}{2}-\cos^2\dfrac{\Theta}{2}\right)^{1/2}}{1+\sin\dfrac{\Theta}{2}}\right]$$

$$I_2 = \int_0^{\phi} \frac{\cos\dfrac{\phi}{2}\, d\phi}{\left[2(\cos\phi-\cos\Theta)\right]^{1/2}} = \sin^{-1}\left(\frac{\sin\dfrac{\phi}{2}}{\sin\dfrac{\Theta}{2}}\right).$$

Applying the operator $\int_0^{\phi}$ to the expressions in (A7) and (A8) corresponding to the iris interval $0 \leqslant \phi < \Theta$ yields the sum formulas

$$\sum_{m=1}^{\infty} P_m(\cos\Theta)\frac{\cos m\phi}{m}$$

$$= \sum_{m=1}^{\infty} \frac{P_m(\cos\Theta)}{m} + I_1$$

$$= -\ln\left\{\sin\frac{\Theta}{2}\left[\cos\frac{\phi}{2}+\left(\cos^2\frac{\phi}{2}-\cos^2\frac{\Theta}{2}\right)^{1/2}\right]\right\}$$

$$\sum_{m=1}^{\infty} P_m(\cos\Theta)\frac{\sin m\phi}{m} = I_2 - \phi = \sin^{-1}\left(\frac{\sin\dfrac{\phi}{2}}{\sin\dfrac{\Theta}{2}}\right) - \phi.$$

With (12′), the asymptotic current sum is

$$\bar{J}_s = 2\sum_{m=1}^{\infty} \frac{\bar{x}_m}{m}\cos m\phi$$

$$= 2\kappa_1 \sum_{m=1}^{\infty} P_m(\cos\Theta)\frac{\cos m\phi}{m}$$

$$+ 2\kappa_2 \sum_{m=1}^{\infty} P_{m+1}(\cos\Theta)\frac{\cos m\phi}{m+1}$$

$$= -2\kappa_2 P_1 + 2[\kappa_1+\kappa_2\cos\phi]\sum_{m=1}^{\infty} P_m(\cos\Theta)\frac{\cos m\phi}{m}$$

$$+ 2\kappa_2\sin\phi \sum_{m=1}^{\infty} P_m(\cos\Theta)\frac{\sin m\phi}{m}$$

$$= -2\kappa_2\cos\Theta - 2[\kappa_1+\kappa_2\cos\phi]$$

$$\cdot\ln\left\{\sin\frac{\Theta}{2}\left[\cos\frac{\phi}{2}+\left(\cos^2\frac{\phi}{2}-\cos^2\frac{\Theta}{2}\right)^{1/2}\right]\right\}$$

$$+ 2\kappa_2\sin\phi\left[\sin^{-1}\left(\frac{\sin\dfrac{\phi}{2}}{\sin\dfrac{\Theta}{2}}\right) - \phi\right]. \quad (15′)$$

APPENDIX IV
FIELD SUM FORMULAS

Consider first the asymptotic H_x field sum, which has the form

$$Q_x = 2\sum_{m=1}^{\infty} \frac{\bar{x}_m}{m}e^{-\alpha m}\cos m\phi$$

$$= -2\kappa_2 P_1 + \kappa_1 \sum_{m=1}^{\infty} \frac{P_m}{m}\left(\lambda_+^m+\lambda_-^m\right)$$

$$+ \kappa_2 \sum_{m=1}^{\infty} \frac{P_m}{m}\left(\lambda_+^{m-1}+\lambda_-^{m-1}\right). \quad (A9)$$

A "generic" sum is immediately recognized and evaluated. Because of the generating function of the Legendre polynomials

$$M(\lambda) \equiv \frac{1}{\sqrt{1-2\lambda\cos\Theta+\lambda^2}} = \sum_{m=0}^{\infty} P_m\lambda^m$$

one obtains

$$\sum_{m=1}^{\infty} P_m\frac{\lambda^m}{m} = \int_0^{\lambda}\frac{d\xi}{\xi}\left(\sum_{m=1}^{\infty} P_m\xi^m\right)$$

$$= \int_0^{\lambda}\frac{d\xi}{\xi}\left(\frac{1}{\sqrt{1-2\xi\cos\Theta+\xi^2}}-1\right)$$

$$= \ln\left(\frac{2}{1-\lambda\cos\Theta+\sqrt{1-2\lambda\cos\Theta+\lambda^2}}\right)$$

$$= K(\lambda). \quad (A10)$$

A combination of (A9) and (A10) yields the asymptotic

sum formula

$$Q_x = \left(\kappa_1 + \lambda_+^{-1} \kappa_2 \right) K(\lambda_+) + \left(\kappa_1 + \lambda_-^{-1} \kappa_2 \right) K(\lambda_-) - 2\kappa_2 P_1.$$

The asymptotic field sums Q_y and Q_z follow in a similar fashion. In particular,

$$Q_y = -\frac{2i\pi}{b} \sum_{m=1}^{\infty} \tilde{x}_m e^{-\alpha m} \cos m\phi$$

$$= -\frac{i\pi}{b} \left[\kappa_1 \sum_{m=1}^{\infty} P_m \left(\lambda_+^m + \lambda_-^m \right) \right.$$

$$\left. + \kappa_2 \sum_{m=2}^{\infty} P_m \left(\lambda_+^{m-1} + \lambda_-^{m-1} \right) \right]$$

$$= -\frac{i\pi}{b} \left\{ \kappa_1 \left[M(\lambda_+) - 1 + M(\lambda_-) - 1 \right] + \kappa_2 \left[\frac{M(\lambda_+)}{\lambda_+} \right. \right.$$

$$\left. \left. - \left(\frac{1}{\lambda_+} + P_1 \right) + \frac{M(\lambda_-)}{\lambda_-} - \left(\frac{1}{\lambda_-} + P_1 \right) \right] \right\}$$

$$= -\frac{i\pi}{b} \left\{ L(\lambda_+) + L(\lambda_-) \right.$$

$$\left. - 2 \left[\kappa_1 + \kappa_2 \left(\cos \Theta + e^\alpha \cos \phi \right) \right] \right\}$$

$$Q_z = \frac{2\pi}{b} \sum_{m=1}^{\infty} \tilde{x}_m e^{-\alpha m} \sin m\phi$$

$$= -\frac{i\pi}{b} \left[\kappa_1 \sum_{m=1}^{\infty} P_m \left(\lambda_+^m - \lambda_-^m \right) \right.$$

$$\left. - \kappa_2 \sum_{m=2}^{\infty} P_m \left(\lambda_+^{m-1} - \lambda_-^{m-1} \right) \right]$$

$$= -\frac{i\pi}{b} \left[L(\lambda_+) - L(\lambda_-) + 2i\kappa_2 e^\alpha \sin \phi \right]$$

where

$$L(\lambda) = \frac{\kappa_1 + \lambda^{-1} \kappa_2}{\sqrt{1 - 2\lambda \cos \Theta + \lambda^2}}. \tag{21}$$

ACKNOWLEDGMENT

REFERENCES

[1] N. Marcuvitz and J. Schwinger, "On the representation of electric and magnetic fields produced by currents and discontinuities in waveguides," J. Appl. Phys., vol. 22, pp. 806–819, 1951.
[2] R. E. Collins, Field Theory of Guided Waves. New York: McGraw-Hill, 1960.
[3] L. Lewin, Advanced Theory of Waveguides. London: Iliffe and Sons, 1951.
[4] L. Lewin, "On the resolution of waveguide discontinuity problems by the use of singular integral equations," IEEE Trans. Microwave Theory Tech., vol. MTT-9, pp. 321–332, July 1961.
[5] L. Lewin and J. P. Montgomery, "A quasi-dynamic method of solution of a class of waveguide discontinuity problems," IEEE Trans. Microwave Theory Tech., vol. MTT-20, pp. 849–852, Dec. 1972.
[6] L. Lewin, Theory of Waveguides. New York: Wiley, 1975.
[7] T. Ruehle and L. Lewin, "The E-plane step–diaphragm junction discontinuity," IEEE Trans. Microwave Theory Tech., vol. MTT-27, pp. 158–160, Feb. 1979.
[8] A. Wexler, "Solution of waveguide discontinuities by modal analysis," IEEE Trans. Microwave Theory Tech., vol. MTT-15, pp. 508–517, Sept. 1967.
[9] P. H. Masterman and P. J. B. Clarricoats, "Computer field-matching of waveguide transverse discontinuities," Proc. Inst. Elec. Eng., vol. 118, pp. 51–63, Jan. 1971.
[10] G. F. VanBlaricum, Jr., and R. Mittra, "Some analytical methods for solving a class of boundary value problems-Part I: Waveguide discontinuities," IEEE Trans. Microwave Theory Tech., vol. MTT-17, pp. 302–309, June 1969.
[11] A. J. Sangster, "Variational method for the analysis of waveguide coupling," Proc. Inst. Elec. Eng., vol. 112, pp. 2171–2179, Dec. 1965.
[12] N. Marcuvitz, Waveguide Handbook (R. L. Series, vol. 10). New York: McGraw-Hill, 1951, p. 374.
[13] J. C. Palais, "A complete solution of the inductive iris with TE_{k0} incidence in rectangular waveguide," IEEE Trans. Microwave Theory Tech., vol. MTT-15, pp. 156–160, Mar. 1967.
[14] J. Schwinger and D. S. Saxon, Discontinuities in Waveguides. London: Gordan and Breach, 1968, ch. III.
[15] R. F. Harrington, Field Computation by the Moment Method. New York: Macmillan, 1964.
[16] T. Vu Khac, "Solutions for some waveguide discontinuities by the method of moments," IEEE Trans. Microwave Theory Tech., vol. MTT-20, pp. 416–418, June 1972.
[17] H. Auda and R. Harrington, "A moment solution for waveguide junction problems," IEEE Trans. Microwave Theory Tech., vol. MTT-31, pp. 515–519, July 1983.
[18] T. E. Rozzi, "Equivalent network for interacting thick conductive irises," IEEE Trans. Microwave Theory Tech., vol. MTT-20, pp. 323–330, May 1972.
[19] T. E. Rozzi and W. F. G. Meccklenbräuker, "Wide-band network modeling of interacting inductive irises and steps," IEEE Trans. Microwave Theory Tech., vol. MTT-23, pp. 235–245, Feb. 1975.
[20] V. M. Pandharipande and B. N. Das, "Coupling of waveguides through large apertures," IEEE Trans. Microwave Theory Tech., vol. MTT-26, pp. 209–212, Mar. 1978.
[21] W. A. Johnson and R. W. Ziolkowski, "The scattering of an H-polarized plane wave from an axially slotted infinite cylinder: A dual series approach," Radio Sci., vol. 19, no. 1, pp. 275–291, Jan. 1984.
[22] R. W. Ziolkowski, "N-series problems and the coupling of electromagnetic waves to apertures: A Riemann–Hilbert approach," SIAM J. Math. Anal., vol. 16, no. 2, pp. 358–378, Mar. 1985.
[23] R. W. Ziolkowski, W. A. Johnson, and K. F. Casey, "Applications of Riemann–Hilbert problem techniques to electromagnetic coupling through apertures," Radio Sci., vol. 19, no. 12, pp. 1425–1531, Dec. 1984.
[24] S. W. Lee, W. R. Jones, and J. J. Campbell, "Convergence of numerical solutions of iris-type discontinuity problems," IEEE Trans. Microwave Theory Tech., vol. MTT-19, pp. 528–536, June 1971.
[25] R. Mittra, T. Itoh, and T.-S. Li, "Analytical and numerical studies of the relative convergence phenomenon arising in the solution of an integral equation by the moment method," IEEE Trans. Microwave Theory Tech., vol. MTT-20, pp. 96–104, Feb. 1972.
[26] T. E. Rozzi and G. de Vrij, "A series transformation for diaphragm-type discontinuities in waveguide," IEEE Trans. Microwave Theory Tech., vol. MTT-20, pp. 770–771, Nov. 1972.
[27] C. Vassallo, "On a direct use of edge condition in modal analysis," IEEE Trans. Microwave Theory Tech., MTT-24, pp. 208–212, Apr. 1976.
[28] K. F. Casey, "Capacitive iris in rectangular waveguide: An exact solution," Lawrence Livermore National Laboratory, UCRL-88377, Oct. 1982.
[29] K. F. Casey, "On the inductive iris in a rectangular waveguide solution," Lawrence Livermore National Laboratory, UCRL-88308, Nov. 1982.
[30] I. N. Sneddon, Mixed Boundary Value Problems in Potential Theory. Amsterdam: North-Holland, 1966.
[31] H. Liska and H. H. Meinke, "Der experimentelle Nachweis der beiden elementaren Typen von Energiewirbeln in Wellenfeldern," Nachrichtentech. Z., Heft 9, pp. 445–448, 1970.

[32] F. Landstorfer, H. Liska, H. Meinke, and B. Müller,
      "Energieströmung in elektromagnetischen Wellenfeldern," *Nach-
      richtentech. Z.*, Heft, 5, pp. 225–231, 1972.
[33] F. Oberhettinger, *Fourier Expansions.* New York: Academic Press,
      1973, pp. 37–38.

lems dealing with the interaction of electromagnetic waves with scattering objects, plasmas, and dielectric materials.

Dr. Ziolkowski is a member of Sigma Xi, Phi Kappa Phi, and the American Physical Society.

✠

✠

Richard W. Ziolkowski was born in Warsaw, NY, on November 22, 1952. He received the Sc.B. degree (with honors) in physics from Brown University in 1974 and the M.S. and Ph.D. degrees in physics from the University of Illinois at Urbana-Champaign in 1975 and 1980, respectively.

He joined the Engineering Research Division at the Lawrence Livermore National Laboratory in 1981 and is currently the Engineering Modeling and Simulation Thrust Area Leader for the Electronics Engineering Department. His research interests include the application of new mathematical methods to linear and nonlinear prob-

J. Brian Grant was born in Tuscon, AZ, in 1958. He received the B.S. and M.S. degrees in electrical engineering in 1981 and 1983, respectively. He is currently pursuing the Ph.D. degree in applied physics at the College of Engineering, University of California, Davis.

In September 1982, he joined the Lawrence Livermore National Laboratory, Livermore, CA, full time after participating in their student summer program for two years. His major responsibilities are the development of analytical and numerical tools for solving electromagnetic problems of importance to the laboratory.